RESEARCH ARTICLE

# The sea-ice detection capability of synthetic aperture radar

**Tao Xie[1, 2*], Li Zhao[1], William Perrie[2] and He Fang[1]**

[1] School of Marine Sciences, Nanjing University of Information Science and Technology, Nanjing, Jiangsu, China
[2] Fisheries & Oceans Canada, Bedford Institute of Oceanography, Dartmouth, Nova Scotia, Canada

**Abstract:** Climate change, increasing activities in areas like offshore oil and gas exploration, marine transport, eco-tourism, in additional to the usual activities of northerners resident are leading to reductions in sea ice. Therefore, there is an urgent need for improvement in the sea ice detection in polar areas. Starting from the mechanism of electromagnetic scattering, based on an empirical dielectric constant model, we apply EM multi-reflection and transmission formulas for coefficients between the air-ice interface and sea water-ice interface to develop a model for estimating the capability of detection of sea ice and ice thickness based on a pulse radar system, synthetic aperture radar (SAR). Although the dielectric constant of sea ice is less than that of sea water, this model can provide a rational methodology as the normalized radar cross section (NRCS) of sea ice is larger than that of sea water due to multiple reflections. The numerical simulations of this model showed that the convergence rate is rapid. With 3 or 4 reflections and transmissions (depending on temperature, salinity, and dielectric constants of sea ice and water), truncation errors can be satisfied using theoretical considerations and practical applications. The model is applied to estimate the capability of SAR to discriminate ice from water. The numerical results suggested that the model ability to measure ice thickness decreases with increasing radar incident angles and increases with increasing radar pulse width. Reflection and transmission coefficients decrease monotonically with ice thickness and are saturated for ice thicknesses above a certain critical value which depends on SAR incidence angle, frequency and dielectric constants of sea ice. The capability to detect ice thickness for given different bands of pulse radar widths can be estimated with this model.

**Keywords:** synthetic aperture radar; sea ice; dielectric constant; normalized radar cross section (NRCS)

*Correspondence to: Tao Xie, School of Marine Sciences, Nanjing University of Information Science and Technology, Nanjing 210044, Jiangsu, China; Email: xtplqk@126.com

**Received**: July 16, 2017; **Accepted**: October 17, 2017; **Published Online**: November 14, 2017

**Citation:** Xie T, Zhao L, Perrie W, *et al*. (2017). The sea-ice detection capability of synthetic aperture radar. *Satellite Oceanography and Meteorology*, 2(2): 261. http://dx.doi.org/10.18063/SOM.v2i2.261

## 1. Introduction

Since the 1980s, the average Arctic summer sea-ice cover has decreased from 7 × 106 km$^2$ to 4.3 × 106 km$^2$ in 2007, reaching a minimum of 3.6 × 106 km$^2$ in 2012. Melting of sea ice is accelerating due to global warming while the Arctic sea ice has an amplification effect on the global climate change (Rahmstorf and Coumou, 2011; Francis and Vavrus, 2012; Huntingford *et al*., 2013; Gao *et al*., 2015). Therefore, the use of aircraft-based and space-based radar for polar sea-ice detection is important for scientific understanding of the climate and related impacts on society.

Synthetic aperture radar (SAR) has the capability for all-weather, all-day observations and can penetrate clouds. Since the first launch of SAR in 1978, it has been applied to earth observations, especially ocean observations, including sea surface wind retrieval (Zhao *et al*., 2013), ocean wave parameters extraction (Xie *et al*., 2015b), ocean front detection (Xie *et al*., 2010; Kuang *et al*., 2012), sea surface oil spill monitoring (Su *et al*., 2016), sea target recognition (Wang *et al*., 2016b), sea-ice movement (Wang *et al*., 2016c) and ice classification (Xie *et al*., 2015a), and other applications. Changes in sea surface roughness caused by various ocean surface features have an effect on the backscattering cross section of SAR sea surface imaging, making it possible to detect these ocean characteristics. Hence, electromagnetic scattering (EMS) of the sea surface for different ocean phenomena has become a hot topic (Zhang *et al*., 2013; Li *et al*., 2014; Xie *et al*., 2016; Komarov *et al*., 2015). Specifically, remote sensing of

sea ice based on SAR is becoming more important. This study focuses on sea-ice classification and ice thickness detection. Artificial neural networks methodologies have been used to identify sea ice (Wang *et al*., 2016a; Rosel *et al*., 2012). However, few studies have been conducted on ice classification based on EMS mechanisms. Sea-ice thickness retrieval has become a bottleneck for climate model research which needs to be resolved. Recently, an empirical relationship between sea-ice salinity and brine volume has been used to study sea-ice thickness but the method is only suitable for detection of thin ice that less than 0.4 m (Zhang *et al*., 2016).

To date, there is still no quantitative theoretical study on the sea-ice detection capability of SAR images. We found two phenomena in the study of sea ice. First, according to the Bragg scattering mechanism, the dielectric constant of sea ice is much smaller than that of sea water. Accordingly, the normalized radar cross section (NRCS) of sea ice should be smaller than that of sea water. However, a large collection of NRCS data of SAR images in Arctic regions shows the opposite result: the NRCS of sea ice is larger than that of sea water even in the marginal ice zone (MIZ). Second, as the thickness of sea ice increases, the NRCS of sea ice becomes smaller. How to interpret and simulate these interesting phenomena in theory are of great significance for the development of sea-ice remote sensing classification and sea-ice thickness retrieval methodologies. Based on the above observations, we develop a model to estimate the capability of SAR for sea-ice detection and estimation of ice thickness.

For the coupled ice-water system, recent studies in marine remote sensing have simplified the problem of EMS at the air-ice interface (Komarov *et al*., 2015; Firoozy *et al*., 2015a). Based on the Bragg scattering model, it is easy to conclude that the radar echo of sea ice should be weaker than that of sea water. However, on the contrary, the radar echo of sea ice is stronger than that of sea water. The reason may be due to the neglected reflection echo of sea water from the bottom side of the sea ice. In fact, the entire system should be seen as a coupled air-ice-water system.

The study of EMS and transmission in the multilayer dielectric structures has been an intensely studied research topic, and the applications are extensive. Originally, the Green's function for multilayer dielectric media was used for the integrated circuit and antenna analysis (Chow *et al*., 1998). With the development of satellite remote sensing technology, the EMS model of multilayer dielectric media became one of the research hotspots in the development of earth observation technology. Franceschetti *et al*. (2008) constructed a multi-layered dielectric with a single rough interface and obtained a first-order perturbation solution of the electric field in the upper half-space of the integration space. Similar research results have been obtained for multi-layer boundary perturbation scattering theory (Imperatore *et al*., 2010, 2012) and volumetric-perturbative reciprocal theory (Imperatore *et al*., 2011) for random rough surfaces and uniform volume integral multilayer dielectric interfaces. Zamani *et al*. (2016a, b) used extended boundary conditions to further study the first-order perturbation solutions of multilayer dielectric media and the second-order perturbation solutions of cross-polarization multi-layer dielectric scattering. Although EMS and transmission of the coupled ice-water interface are the simplest multi-layer structure interface problems, thus far, research on the EM echo signal related to sea ice has not seen significant advances.

The related research is divided into two main categories. The first category is the EMS model of the air-ice interface. Golden *et al*. (1998) divided the ice layer into pure ice layer and brine ice, and calculated the equivalent permittivity of the ice layer according to the dielectric constant model of the sea-ice microstructure. Based on the theory of radiative transfer (RT) and the distorted wave Born approximation, the EMS model of the air-ice interface was established. The model can be used to calculate radar cross sections of one-year and multi-year ice. The finite difference time domain method (FDTD) (Nassar *et al*., 2000) and finite volume time domain algorithm (FVTD) (Isleifson *et al*., 2012) were used to establish the EMS numerical model of the air-ice interface, in which the dielectric constant of sea ice was determined by the Polder-Van Santen-de Loor (PVD) model. Based on the first type of research, the second type took the snow cover into account. Komarov *et al*. (2014) first used the first-order approximation and perturbation method to establish a non-uniform boundary surface EMS model and applied it to the snow-covered sea ice. Thus, the model was used to construct the C-band radar backscattering model (Engen and Johnsen, 1995). The sea-ice dielectric constant, sea-ice temperature and salinity were reconstructed by multi-band and multi-polarization NRCS data (Firoozy *et al*., 2015b, 2016).

According to the existing literature, the EMS model of sea ice mainly solves the problem of the numerical calculation for EMS in the case of uneven stratification and snow cover on the ice layer, ignoring the study of the ice-thickness detection using a model based on SAR. In this paper, we use the EMS and transmission theory of multilayer dielectric structures to explain the mechanism whereby the NRCS of sea ice from SAR imagery is larger than that of sea water in Arctic regions. Moreover, a model estimating the capability of SAR to detect sea ice is put forward in this paper.

The second part of this paper presents a model for

the relative sea-ice dielectric constant, based on sea-ice thickness. In the third part, a model for the EM multi-reflection and transmission of sea ice is established, based on ice thickness. According to this analysis, a model is developed to estimate ice thickness based on the pulse system radar. In the fourth part, relevant numerical results are given according to the established model. Finally, the conclusions are presented in the last part of the paper.

## 2. Relative Dielectric Constant of Sea Ice

When microwave radar is used to observe the ocean, the material properties (mainly the dielectric constant) of the sea surface play a key role in the EM reflection and transmission. This is the main mechanism for the SAR image to distinguish the surface of different materials. The dielectric constant of sea ice (especially first-year ice) is affected by sea-ice brine volume, salinity, sea-ice temperature, and related variables. Therefore, it is necessary to obtain a relationship between the dielectric constant and sea-ice thickness before establishing a model for sea-ice EM reflection and transmission.

For high-frequency EM waves, the dielectric constant of sea ice can be expressed as (Vant *et al*., 1978; Arcone *et al*., 1986):

$$\varepsilon_{ice} = \varepsilon' + j\varepsilon'' \tag{1}$$

where $\varepsilon' = 3.05 + 0.0072f_{vb}$, $\varepsilon'' = 0.02 + 0.0033f_{vb}$. The brine volume is:

$$f_{vb} = \frac{\rho_{ice} S_{ice}}{F_1(T_{ice}) - \rho_{ice} S_{ice} F_2(T_{ice})} \tag{2}$$

where $\rho_{ice} = 0.917 - 1.403 \times 10^{-4} T_{ice}$, $\rho_{ice}$ is sea-ice density, $T_{ice}$ is sea-ice temperature in °C. $F_1$ and $F_2$ can be obtained by the formulas (3) and (4) according to the parameters in Table 1 (Vant *et al*., 1978; Arcone *et al*., 1986).

$$F_{1,2}(T_{ice}) = \alpha_0(F1,2) + \alpha_1(F1,2)T_{ice} + \alpha_2(F1,2)T_{ice}^2 + \alpha_3(F1,2)T_{ice}^3 \tag{3}$$

Sea-ice salinity can be expressed as a function of sea-ice thickness (Cox and Weeks, 1983):

$$S_{ice} = \begin{cases} 7.88 - 1.59h_{ice} & h_{ice} > 0.4\text{m} \\ 14.24 - 19.39h_{ice} & h_{ice} \ll 0.4\text{m} \end{cases} \tag{4}$$

where $h_{ice}$ is sea-ice thickness.

**Table 1.** Coefficients $\alpha_0$, $\alpha_1$, $\alpha_2$ and $\alpha_3$ for functions of equations (3)

| Coefficients | $-30 \le T_{ice} \le -22.9$ °C | | $-22.9 \le T_{ice} \le -2$°C | |
|---|---|---|---|---|
| | $F_1(T_{ice})$/mg·m$^{-3}$ | $F_2(T_{ice})$/mg·m$^{-3}$ | $F_1(T_{ice})$/mg·m$^{-3}$ | $F_2(T_{ice})$/mg·m$^{-3}$ |
| $\alpha_0$ | 9899 | 8.547 | −4.732 | 0.08903 |
| $\alpha_1$ | 1309 | 1.089 | −22.45 | −0.01763 |
| $\alpha_2$ | 55.27 | 0.04518 | −0.6397 | −0.000533 |
| $\alpha_3$ | 0.716 | 0.0005819 | −1.01074 | −0.000008801 |

## 3. Model for Estimating the Limit for Detection of Sea Ice and Estimation of Ice Thickness

### 3.1 Electromagnetic Multi-reflection and Transmission Coefficients

As shown in Figure 1, the sea-ice thickness is h. The dielectric media 1, 2 and 3 are air, sea ice and sea water, respectively. Their dielectric constants, permeabilities and conductivities are ($\varepsilon_1$, $\mu_1$, $\sigma_1$), ($\varepsilon_2$, $\mu_2$, $\sigma_2$) and ($\varepsilon_3$, $\mu_3$, $\sigma_3$), respectively. In general, in addition to ferromagnetism, the permeability of other media is approximately equal to the permeability in a vacuum, *i.e.*, $\mu_1 = \mu_2 = \mu_3 = \mu_0$. In air, $\varepsilon_1 = \varepsilon_0$, $\sigma_1 = 0$. The permeability $\mu_0$ and dielectric constant $\varepsilon_0$ in a vacuum are equal to $4\pi \times 10^{-7}$ H/m and $8.85419 \times 10^{-12}$ F/m, respectively. The sea-ice conductivity $\sigma_2$ is equal to $\omega\varepsilon''\varepsilon_0$, where the angular frequency $\omega$ of the EM wave is equal to $2\pi f$ and f is the frequency of the EM wave. The conductivity of sea water can be written as:

$$\sigma_3 = 0.086374 + 0.030606T_w - 0.0004121T_w^2 + S_w(0.077454 + 0.001687T_w + 0.000019371T_w^2) \tag{5}$$

where $S_w$ and $T_w$ are salinity and temperature of sea water, respectively. The Debye model function (Ellison *et al*., 1998) of the sea water dielectric constant is:

$$\varepsilon_3 = \varepsilon_\infty + \frac{\varepsilon^* - \varepsilon_\infty}{1 + (2\pi f\tau)^2} + i\left(\frac{2\pi f\tau(\varepsilon^* - \varepsilon_\infty)}{1 + (2\pi f\tau)^2} + \frac{\sigma_3}{2\pi f\varepsilon_0}\right) \tag{6}$$

where,

$$\varepsilon_\infty = 6.4857 - 0.04203T_w - 0.006588T_w^2 + 0.0006492T_w^3 - 1.2328 \times 10^{-5}T_w^4 + 5.0433 \times 10^{-8}T_w^5 \tag{7}$$

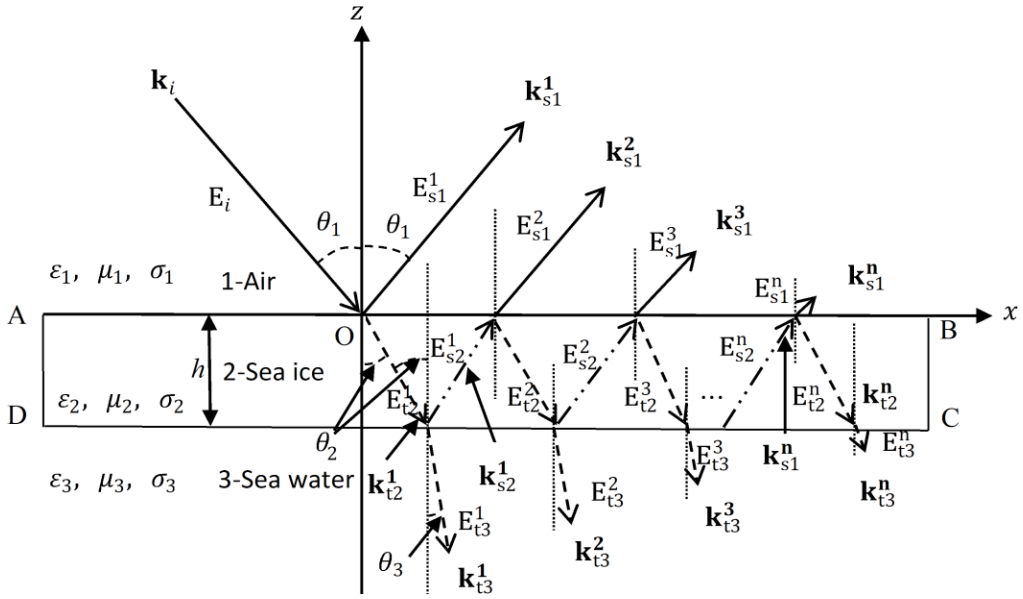


**Figure 1.** Schematic diagram of multi-reflections and transmissions is described for a plane electromagnetic wave that is incident on the surface of ice plate with thickness h.

The relaxation time, τ associated with temperature and salinity is:

$$\tau = 17.03 - 0.66651T_w + 5.1482 \times 10^{-3}T_w^2 + 1.2145 \times 10^{-3}T_w^3 - 5.0325 \times 10^{-5}T_w^4 + 5.8272 \times 10^{-7}T_w^5 + S_w(-6.772 \times 10^{-3} + 2.357 \times 10^{-4}T_w + 5.075 \times 10^{-4}T_w^2 - 6.3983 \times 10^{-5}T_w^3 + 2.463 \times 10^{-6}T_w^4 - 3.0676 \times 10^{-8}T_w^5) \quad (8)$$

$$\varepsilon^* = a' + a''S_w \quad (9)$$

where,

$$a' = 81.82 - 6.0503 \times 10^{-2}T_w - 3.1661 \times 10^{-2}T_w^2 + 3.1097 \times 10^{-3}T_w^3 - 1.1791 \times 10^{-4}T_w^4 + 1.4838 \times 10^{-6}T_w^5 \quad (10)$$

$$a'' = 0.12544 + 9.4037 \times 10^{-3}T_w - 9.5551 \times 10^{-4}T_w^2 + 9.0888 \times 10^{-5}T_w^3 - 3.6011 \times 10^{-6}T_w^4 + 4.71 \times 10^{-8}T_w^5 \quad (11)$$

Considering the case of airborne radar or satellite remote sensing, the incident EM wave arriving at the sea-ice surface can be approximated as a plane wave. Therefore, it may be represented as:

$$E_i = E_0 e^{-j(k_i \cdot r - \omega t)} \quad (12)$$

where r is the space position vector (x, y, z) and t is time. The angular frequency, ω is equal to 2πf, where f is the frequency of the incident EM wave. The incident angle of the plane EM wave and the reflection angle in air are $\theta_1$. The incident plane is xoz and the y-direction is inward, perpendicular to the page. The unit vector of the coordinate axis is supposed to be ($x_0$, $y_0$, $z_0$). Thus, the incident wave vector is:

$$k_i = k_0(\sin\theta_1 x_0 - \cos\theta_1 z_0) \quad (13)$$

where $k_0$ is wave number of incident EM wave with wavelength $\lambda_0$ and $k_0$ is equal to $2\pi/\lambda_0$. The first reflected wave vector in the air can be expressed as:

$$k_{s1}^1 = k_0(\sin\theta_1 x_0 + \cos\theta_1 z_0) \quad (14)$$

In the air-ice (AB) interface, in addition to reflection, the energy of the EM wave is partly transmitted into the sea ice and the transmission angle is $\theta_2$. The transmission wave number is:

$$k_{t2}^1 = k_2(\sin\theta_2 x_0 - \cos\theta_2 z_0) \quad (15)$$

According to Maxwell's equation for the boundary AB, the boundary condition of the EM field and the plane wave solution, it is easy to prove that $k_2$ is equal to $k_0$. At the same time, $\theta_1$ and $\theta_2$ should satisfy the refraction law relation:

$$\sin\theta_2 = \sqrt{\frac{\varepsilon_1}{\varepsilon_2}}\sin\theta_1 \quad (16)$$

The reflected electric field is:

$$E_{s1}^1 = E_{s10}\exp\left(-j(k_{s1}^1 \cdot r' - \omega t)\right) \quad (17)$$

Considering the decay process of EM waves in sea ice and sea water, the EM wave attenuation coefficient in sea ice is given as follows:

$$E_{t2}^1 = E_{t20}\exp(-\alpha_2 r_2)\exp\left(-j\left(k_{t2}^1 \cdot r'' - \omega t\right)\right) \quad (19)$$

After the EM wave spreads over $r_2$ distance in the sea ice, the transmission electric field can be written as:

$$E_{t2}^{1} = E_{t20}\exp(-\alpha_2 r_2)\exp\left(-j\left(k_{t2}^{1}\cdot r'' - \omega t\right)\right) \quad (19)$$

As can be seen from Figure 1, this result gives:

$$r_2 = \frac{h}{\cos\theta_2} \quad (20)$$

According to the boundary conditions and the Fresnel formula, one can obtain the relationship among incident, reflected and transmitted wave amplitudes. Thus, we can get the reflection coefficient, F and transmission coefficient, T of the interface. For each wave vector, there are two independent polarization states: horizontal polarization (H polarization: E is parallel to the incident plane) and vertical polarization (V polarization: E is perpendicular to the incident plane). They follow different laws on the border. Mathematical induction is used to derive the EMS and transmission model of sea ice for horizontal polarization and vertical polarization in the MIZ (specific parameters are shown in Figure 1). The index n of the following parameters means the nth time that the EM wave encounters different media interfaces (AB or CD interface) during its propagation. In the parameter subscripts, H is horizontal polarization, V is vertical polarization, m and n are the dielectric layers, equal to 1, 2 and 3. Here, mn indicates that EM waves propagate from the dielectric layer, m into the dielectric layer, n. The derivation of coefficients for EM multi-reflection and transmission events in the air-ice-water multilayer dielectric structure is given in the Appendix.

According to the results of the Appendix, the reflection coefficient of the air-ice interface for horizontal polarization is:

$$S_{HH} = a + \frac{bek}{1+aeexp(-2\alpha_2 r_2)} \quad (21)$$

For vertical polarization, we have:

$$S_{VV} = c + \frac{dgl}{1+cgexp(-2\alpha_2 r_2)} \quad (22)$$

The transmission coefficient of the ice-water interface for horizontal polarization is:

$$T_{HH} = \frac{bfexp(-\alpha_2 r_2)}{1+aeexp(-2\alpha_2 r_2)} \quad (23)$$

For vertical polarization, we have:

$$T_{VV} = \frac{djexp(-\alpha_2 r_2)}{1+cgexp(-2\alpha_2 r_2)} \quad (24)$$

### 3.2 Detectable Ice Thickness Limit and Sea-ice Recognition Degree

For a pulse system radar, the width of the pulse signal is $\tau$ and the velocity of the EM wave is $c_0$. Thus, the thickness of sea ice that can be detected with limited pulse width is:

$$h_{cri} = \frac{c_0\tau\cos(\theta_2)}{2} \quad (25)$$

For estimation of ice thickness, in addition to considering the pulse width limitation, it is necessary to consider the distinction between the NRCS of sea ice and that of the environment (sea water). The reflection coefficient of the air-ice interface for horizontal polarization is:

$$S_{HH,h_{cri}} = a + \frac{bek}{1+aeexp(-c_0\alpha_2\tau/\cos(\theta_2))} \quad (26)$$

For vertical polarization, the reflection coefficient can be written as:

$$S_{VV,h_{cri}} = c + \frac{cgl}{1+cgexp(-c_0\alpha_2\tau/\cos(\theta_2))} \quad (27)$$

For the sea surface with no ice, the reflection coefficients of the air-ice interface for horizontal and vertical polarizations are:

$$S_{HH,water} = \frac{\tan(\theta_1-\theta)}{\tan(\theta_2+\theta)} \quad (28)$$

$$S_{VV,water} = \frac{\sin(\theta_1-\theta)}{\sin(\theta_1+\theta)} \quad (29)$$

where $\theta$ can be written as:

$$\theta = \operatorname{asin}\left(\sqrt{\frac{\varepsilon_1}{\varepsilon_3}}\sin\theta_1\right) \quad (30)$$

In this paper, the concept of sea-ice "recognition degree" is defined as the discrepancy of the NRCS between sea water and sea ice, which is represented by $D_{ice}$. The physical meaning is that the degree of discrimination between the sea-ice region and the sea water region in the radar scattering image, and the sea-ice recognition degree for horizontal and vertical polarizations, are respectively:

$$D_{HH,ice} = \frac{S_{HH,water}}{S_{HH,h_{cri}}} - 1 \quad (31)$$

$$D_{VV,ice} = \frac{S_{VV,water}}{S_{VV,h_{cri}}} - 1 \quad (32)$$

That means the two media cannot be distinguished. Moreover, the greater the absolute value of D, the greater the degree of sea-ice recognition. Thus, it is easier to distinguish sea ice from seawater.

At present, we developed a model to estimate sea-ice detection, using the pulse system radar, *i.e.*, the formulas (25), (31) and (32), which can also be used to estimate the limit to which we can estimate sea-ice thickness and the degree of sea-ice recognition.

## 4. Numerical Results and Analysis

### 4.1 Characteristics of Sea-ice Reflection and Transmission Coefficients

In this paper, as shown in Figure 1, the thickness of the floating sea-ice model is h. When h is equal to 0, it means there is no sea ice on the sea surface. The EM pulse sequence of SAR carried by RADARSAT-2 is used as the incident wave. The bandwidth of the radar pulse is $3.00 \times 10^7$ Hz. The speed of light and the frequency of the radar are $3 \times 10^8$ m/s and $5.04 \times 10^9$ Hz, respectively. The temperature of sea ice and sea water are set to −2 °C and 0 °C, respectively.

Firstly, the convergence of the model is studied numerically. In Figure 2, the relative truncation errors of reflection and transmission coefficients vary with the number of reflections and transmissions. The radar incidence angle is 45° and sea-ice thickness is 1 m. The salinity of seawater is 35 psu. A large number of numerical results show that as the number of reflections and transmissions increases, truncation errors of the coefficients decrease rapidly and tend to zero. When the number is 4, truncation errors of the reflection coefficient (transmission coefficient) for VV polarization and HH polarization are 0.8% (0.3%) and 0.06% (0.006%), respectively. Compared with the case of only one reflection and truncation, errors of the reflection coefficient (transmission coefficient) for VV polarization and HH polarization are 59.3% (20.3%) and 79.9% (8.3%), respectively. The results show that the model converges quickly. If the requirement for truncation errors is relatively low (less than 5%), the three times reflection and transmission are enough to satisfy the accuracy requirements.

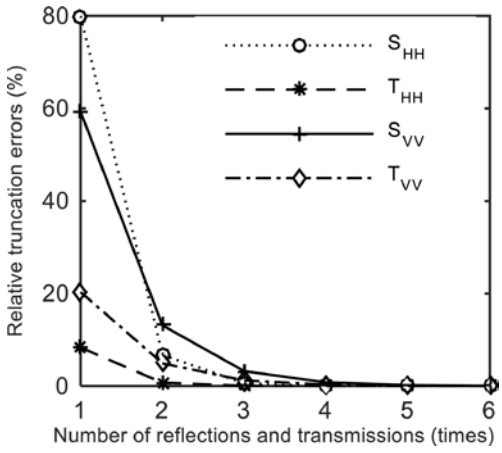


**Figure 2.** Relative truncation errors in terms of the number of reflections and transmissions.

Figure 3 shows the changes of reflection and transmission coefficients varying with the number of reflections and transmissions corresponding to Figure 2. The results show that when this number increases, the reflection and transmission coefficients increase rapidly and tend to their corresponding saturation values.

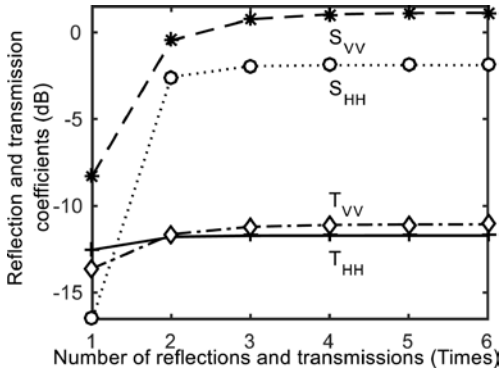


**Figure 3.** Reflection and transmission coefficients in terms of the number of reflections and transmissions.

Secondly, based on the convergence of the model, it is necessary to simulate the changes of reflection and transmission coefficients varying with radar incidence angles. Considering that current space-borne SAR instruments mainly adopt medium incidence angles (from 20° to 50°), the incidence angles change from 0° to 50°. Thus, the model established previously is used to simulate the changes of the reflection and transmission coefficients of the EM wave with respect to incidence angles.

Figure 4 shows the results of the variation of reflection and transmission coefficients with incidence angles. This figure does not consider the situation of multi-reflections and refractions. The variation of reflection and transmission coefficients errors with incidence angles are shown in Figure 5. For the case of small incidence angles (from 0° to 10°), the reflection and transmission coefficients and their corresponding errors are only slightly affected by the polarization state. When incidence angles are in the medium range, the reflection and transmission coefficients decrease with increases of the incidence angles for VV and HH polarizations. Reflection and transmission coefficients for VV polarization are larger than those for HH polarization at the same incident angles. Thus, the discrepancy of reflection and transmission coefficients between VV polarization and HH polarization becomes larger with increasing incident angles, which is consistent with descriptions in the literature. Without considering the case of multi-reflections and refractions, the errors of reflection and transmission coefficients will decrease with increases in the incident angles. Compared with the reflection coefficient where there is no ice (Figure 4), and considering multi-reflections, the reflection coefficient of sea ice is larger than that of sea water for VV polarization. This is because the presence of sea

ice makes the sea surface form multi-reflections and refractions, thereby enhancing the intensity of the spatial echoes. Sea water has a large electrical conductivity and the skin depth is small; so multi-reflection and refraction effects will not form.

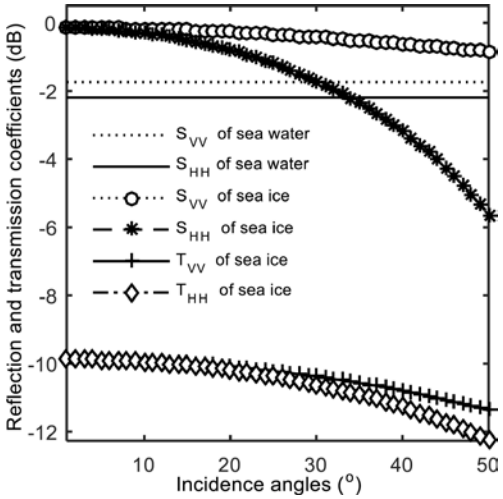


**Figure 4.** Reflection and transmission coefficients in terms of incidence angles.

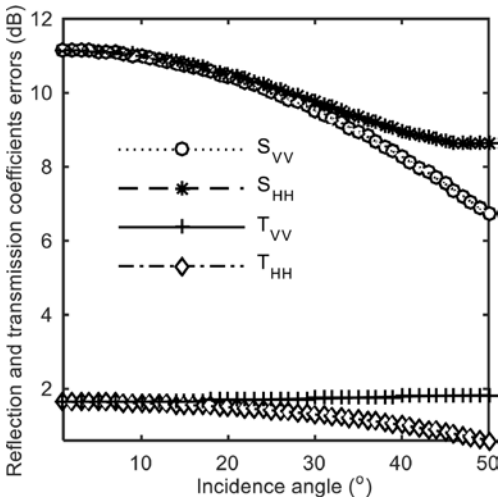


**Figure 5.** Reflection and transmission coefficients errors in terms of incidence angle.

Finally, the effect of sea-ice thickness on the reflection and transmission coefficients is numerically studied. At present, remote sensing applications mainly use pulse radar systems and the pulse width (units: seconds) determines the temporal and spatial resolution of the target, thus affecting the SAR image quality. The pulse signal bandwidth of RADARSAT-2 SAR is used and its value is $3.00 \times 10^7$ Hz. Let the sea-ice thickness increase from 0 to 15 m, and let the incident angle be 20°. Thus, the reflection and transmission coefficients of the EM wave variation with sea-ice thickness are shown in Figure 6. Figure 7 shows the variations of reflection and transmission coefficient errors of the EM wave with sea-ice thickness without considering multi-reflections and refractions and their effects.

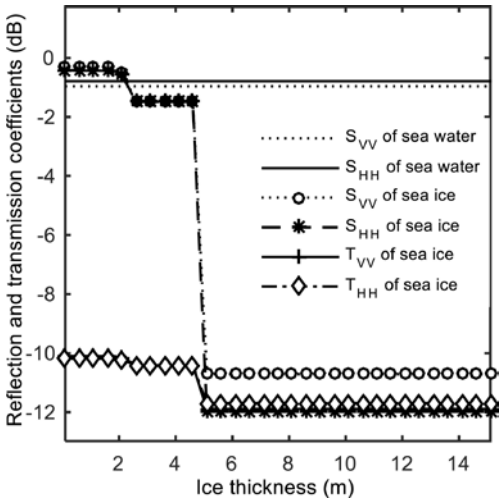


**Figure 6.** Reflection and transmission coefficients in terms of ice thickness.

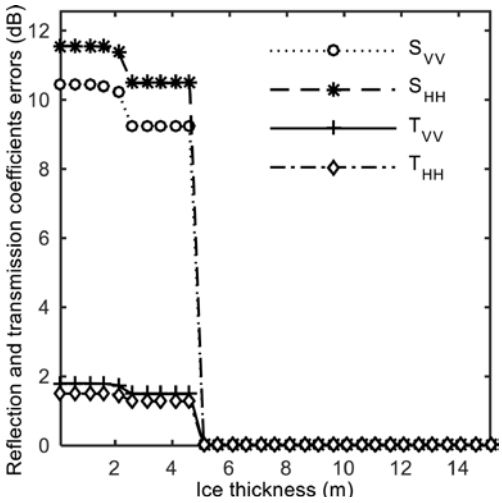


**Figure 7.** Reflection and transmission coefficients errors in terms of ice thickness.

Figure 6 shows that when the sea-ice thickness is less than a certain threshold (2.6 m in the figure), the reflection coefficient in the presence of sea ice is larger than that in the case without ice. This result is consistent with our study of the phenomena observed by the NRCS intensity images in Arctic sea ice. This also explains why the dielectric constant of the sea ice (relative permittivity is about 3, depending on temperature and salinity) is much smaller than that of sea water (relative permittivity is about 80, depending on temperature and salinity). By comparison, in the Arctic region, the NRCS of sea water is smaller than that of sea ice. This is because the sea-ice thickness of most of the Arctic region is less than 2 m and the presence of sea ice makes it possible to form

multi-reflections. Therefore, the SAR can receive the second, third…, nth echo, with the result that the SAR image intensity of sea ice is larger than that of sea water. When the sea-ice thickness exceeds a critical value (5 m in Figure 6 and 7 m in Figure 7), the reflection and transmission coefficients and their errors will not change any more. Because this result is based on this incident angle, the radar echo will exceed the pulse reception range when sea-ice thickness is beyond the critical value. The critical values of the above sea-ice thickness limitation are related to incident angles and the dielectric constant of sea ice and seawater.

It can also be seen from Figure 6 and Figure 7 that the reflection and transmission coefficients and their errors decrease sharply with increasing sea-ice thickness. This is mainly affected by the radar pulse width. The greater the radar pulse width, then the EM waves can pass through thicker sea ice in the same pulse width (shown in Figure 8).

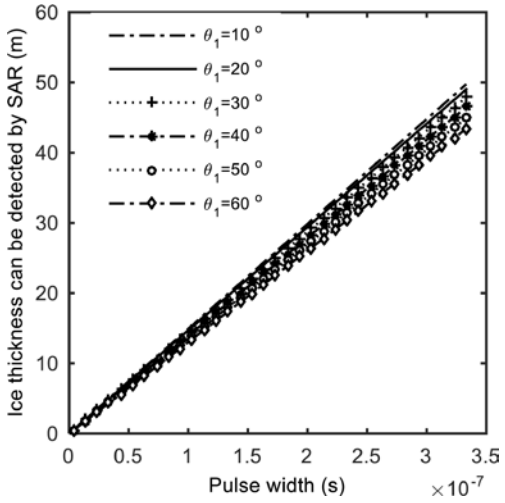


**Figure 8.** The detectable ice thickness in terms of SAR pulse width.

## 4.2 Characteristics of Sea-ice Thickness Detection Limits and Its Recognition Degrees

We can evaluate the sea-ice detection capability of the radar system with respect to two aspects of the problem by using the physical model to estimate the ice detection capability of the pulse system radar.

First, detecting the ice thickness can be evaluated. Figure 8 simulates the variation of sea-ice thickness with the radar pulse width. The results show that when the width of the pulse signal increases from $3.33 \times 10^{9}$ s to $3.33 \times 10^{7}$ s, the detectable ice thickness increases linearly from 0.5 m to 50 m, and is affected by the incident angles. This means that a radar system with a small pulse width detects a smaller thickness of sea ice than that with a large pulse width. For example, the pulse signal bandwidth of RADARSAT-2 SAR is $3.0024403 \times 10^{7}$ Hz and the corresponding pulse width is $3.3306 \times 10^{-8}$ s. When the incident angle is 30°, the detectable ice thickness is 4.78 m. When the corresponding pulse width is $3.3306 \times 10^{7}$ s, the detectable ice thickness is 47.87 m.

Figure 9 shows the results of the variation of the detection capability for sea-ice thickness with respect to incident angles, increasing from 2° to 60°. The results show that when the incident angle increases, the limit in the detectable ice thickness becomes smaller. This is because increases in incident angles result in increases of transmission angles at the boundary AB and on the refection angles at boundary CD. For fixed radar pulse bandwidth, if the detectable ice thickness is invariant, the echo will exceed the receiving pulse width. Therefore, only when the limit on the detectable sea-ice thickness becomes relatively small, can the echo be received by the receiver in the same radar pulse width.

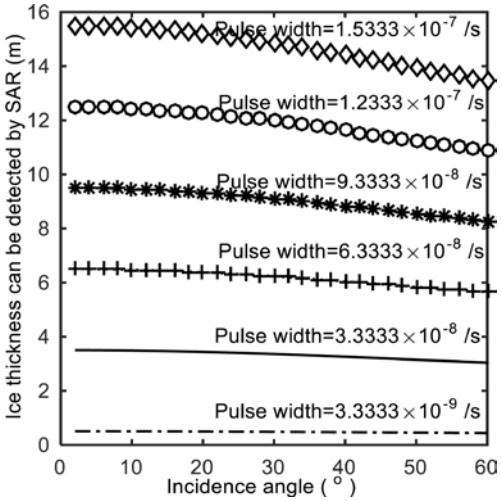


**Figure 9.** The SAR detection of ice thickness in terms of incidence angle.

Second, our model can be used to evaluate the ability of the radar to recognize sea ice from sea water in SAR images. Formulas (32) and (33) can be used to quantitatively calculate the sea-ice identification ability of HH and VV polarizations, respectively.

Figure 10 shows the simulated results for the capability of the radar to discriminate sea ice as a function of radar frequency using our established physical model. As the radar frequency increases from 1 GHz to 9000 GHz (for clarity in Figure 10, only 1–900 GHz is shown), the radar discrimination capability for sea ice decreases exponentially. When the radar frequency exceeds 200 GHZ, the radar capability for discrimination of sea ice for HH and VV polarizations begins to converge to 0.45 and 0.34, respectively. Figure 11 shows the effect of incident angles on the radar capability for discrimination

of sea ice. It can be seen from Figure 10 and Figure 11 that the radar capability for discrimination of sea ice for HH polarization is larger than that of VV polarization and this difference is not affected by the radar frequency. With increased incident angles, the radar capability for discrimination of sea ice for HH polarization increases, whereas it decreases for VV polarization.

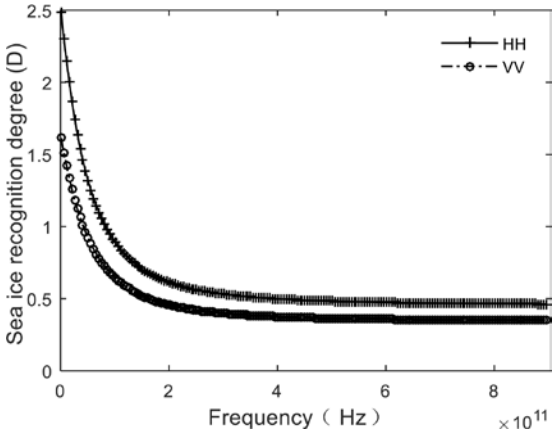


**Figure 10.** Sea-ice recognition degree in terms of frequency.

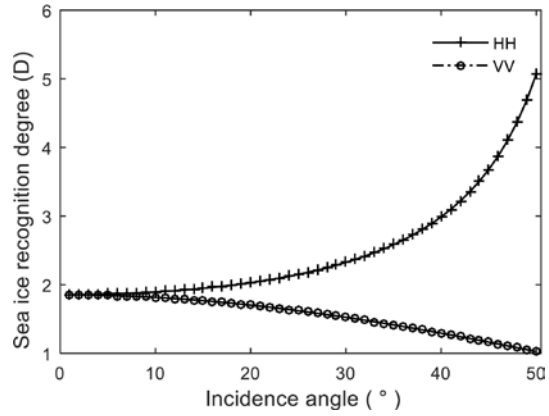


**Figure 11.** Sea-ice recognition degree in terms of incidence angle.

Results of the study of the capability of the radar model for discrimination of sea ice are compared to field observations in Figure 10 and Figure 11. Gade *et al*. (1998) used the L-band, C-band, and X-band SAR images to observe the same imagery (the difference among different types of sea ice is the thickness and dielectric constant) covering the sea surface area and studied the attenuation ratio parameters of different polarization cases. In our model, this is the ratio of the NRCS of the image to that of sea water in the SAR image, corresponding to $DR_{pp}$. The relationship between the radar capability for sea-ice discrimination, relating $D_{pp}$ and $DR_{pp}$, is:

$$DR_{PP} = \frac{1}{D_{pp}+1} \tag{33}$$

where pp denotes the polarization mode (HH or VV). Gade *et al*. (1998) compared SAR images of different bands and polarization modes and found that the attenuation ratio $DR_{pp}$ of low frequency radar (such as L band) is smaller than that of high frequency radar (such as X band) (see Figure 4, Figure 6 and Figure 7 in Gade *et al*. (1998). It can be seen from equation (33) that the radar discrimination capability $D_{pp}$ of the low frequency radar band is higher than that of the high frequency radar band.

Similarly, it can also be found from Figure 4, Figure 6 and Figure 7 in Gade *et al*. (1998) that the attenuation ratio $DR_{HH}$ of HH polarization is less than that of VV polarization. Accordingly, the radar discrimination capability $D_{HH}$ of HH polarization is higher than $D_{VV}$ of VV polarization.

Finally, we have shown through the above results and comparisons, that our physical model is consistent with the observations. Previous observations can also be methodically interpreted by using our physical model. According to our model, the dielectric constant, radar wavelength and incident angles are the main factors that affect the radar echo because of the multi-scattering contributions.

## 5. Sea-ice Recognition Degrees in SAR Images

To validate and show the sea-ice recognition ability of SAR, a set of SAR images covering sea ice and water are studied here. The selected quad-polarization RADARSAT-2 SAR images were captured during the Labrador shelf pack ice and iceberg survey from March 17 to March 21, 2011. As an example, Figure 12 shows the SAR images which were captured at 9:55:58, on March 20, 2011. The center of the backscattering image is (55˚8'7"W, 58˚22'43"N). The polarization modes of SAR images (backscattering coefficients) have shown in Figure 12.

Following equation (33), the degree of recognition of sea ice in SAR images of HH polarization and VV polarization is shown in Figure 13. In Figure 13, the degree of recognition of sea ice varies with respect to the roughness of the ice surface. The effects of sea-ice surface roughness on the degree of recognition of sea ice are not considered here and will be included in our future work.

Comparing the results of the degree of recognition of HH and VV polarization SAR images shown in Figure 13 with our idea model results shown in Figure 11, one can find that numerical results of our model are in good agreement with results from SAR measurements. In Figure 13, the mean values of the degree of recognition of sea ice in HH and VV polarization SAR images are $\overline{DR_{HH}}$−5.14 and $\overline{DR_{VV}}$−1.76, respectively. The incidence angle of the SAR images is 49° in Figure 12. The numerical results of the degree of recognition of sea

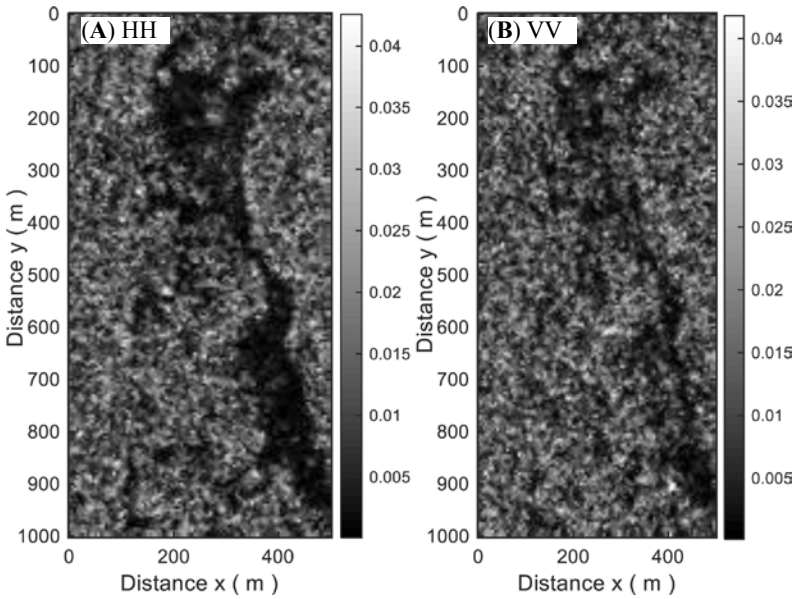


**Figure 12.** Backscattering coefficients of SAR images in different polarizations. SAR images were captured at 9:55:58, on March 20, 2011. The center of the backscattering image is (55˚8'7"W, 58˚22'43"N). (**A**) HH polarization; (**B**) VV polarization. RADARSAT-2 Data and Products from MacDonald, Dettwiler, and Associates Ltd. All Rights Reserved.

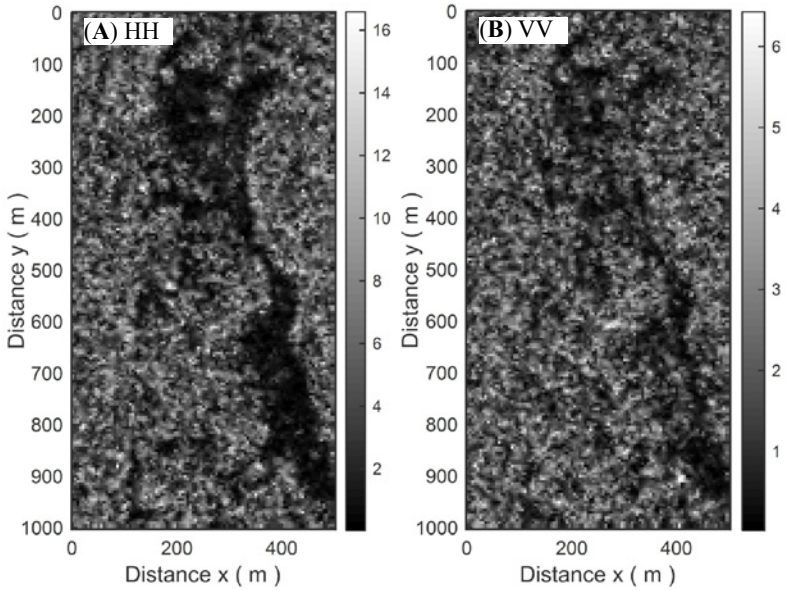


**Figure 13.** Degree of sea-ice recognition in SAR images. (**A**) $DR_{HH}$ in HH polarization; (**B**) $DR_{VV}$ in VV polarization.

ice in HH and VV polarization SAR images are 4.70 and 1.10 at incidence angle 49°. These results imply that numerical values of the degree of recognition of sea ice in HH polarization is larger than those of VV polarization as validated by SAR measurements shown in Figure 13. The discrepancy of the mean degree of recognition of sea ice between HH polarization and VV polarization SAR images is 3.38 while the discrepancy of the degree of recognition of sea ice for our model result is 3.6. Thus, our model has high accuracy for sea-ice recognition.

## 6. Conclusions

This paper focuses on the EM multi-reflection and transmission coefficients of floating sea ice, based on the sea-ice conductivity model and on sea-ice thickness. We have put forward the concept of a model for the capability of radar for the discrimination of sea ice and water. In addition, we established a physical model for ice detection using a pulse radar system.

The results show that the convergence rate of the model is quite rapid. Generally, 3 to 4 reflections and

transmissions can satisfy the calculation and application requirements. The results of this model successfully explain that when ice thickness is less than a certain critical value, the NRCS of sea water is smaller than that of sea ice, based on multi-reflections in the ice layer. When the ice thickness is greater than a secondary critical value, the NRCS does not change as the sea-ice thickness increases. This is because when the ice layer is beyond the critical thickness, the time for the processes related to EM wave reflection, transmission and refraction exceeds the radar pulse width, and therefore the corresponding multi-reflection echoes are no longer received by the radar receiver within the same pulse width.

Based on the physical model, the capability of the radar for the detection of sea ice can be evaluated with regard two factors: one is the radar discrimination of sea ice from open water and the other is the detection of ice thickness. Numerical results show that the radar discrimination capability of sea ice decreases exponentially with increases in radar frequency, and the ability of HH polarization radar is higher than that of VV polarization radar. The results are in agreement with observations captured in the SAR images in the literature and also, a test case SAR image captured during the Bedford Institute of Oceanography (BIO) survey of the Labrador shelf pack ice and icebergs on March 20, 2011.

In summary, this paper uses a new numerical simulation model and we can suggest the following main conclusions: (1) The new EM scattering and transmission model of floating sea ice, based on ice thickness, has been successfully applied to explain that the NRCS of the sea ice is higher than that of the sea water. That is, the multi-scattering between the air-ice interface and the ice-water interface makes the EM echo signal received in the same pulse width stronger than the sea surface radar echo, and the corresponding radar signal transmitted from seawater is smaller. (2) Radar scattering and transmission coefficients are affected by incident angles. As the incident angle increases, scattering and transmission coefficients of the VV and HH polarizations become smaller. (3) Due to the influence of the existing pulsed radar system, the reflection and transmission coefficients and their errors decrease sharply with increases in sea-ice thickness. (4) As the radar frequency increases, the radar capability for discrimination of sea ice decreases exponentially; and the capability of HH polarization radar is higher than that of VV polarization radar. (5) The physical model for the capability for ice detection for the pulse system radar can be used to explain the observation results obtained by SAR.

In addition to successfully explaining the existing sea-ice remote sensing phenomena (detection) and estimating ice thickness for the pulse system radar, the model can be used to further develop the fully polarimetric (VV/HH/VH /HV) EMS model for the rough sea-ice surface and explore the problem for sea-ice classification.

## Conflicts of Interest

The authors declare no conflict of interest.

## Acknowledgments

This project is supported by the National Key Research and Development Program of China (2016YFC1401007), the Global Change Research Program of China (Grant No. 2015CB953901), the National Natural Science Foundation of China (41776181) the Canadian Program on Energy Research and Development (OERD), and the Office of Naval Research (Code 322, "Arctic and Global Prediction", Grant number and Principal Investigator: William Perrie, N00014-15-1-2611).

## Appendix

In this section, we present expression for EM multi-reflection and transmission coefficients of air-ice-water multilayer dielectric structure. The specific process is as follows:

For horizontal polarization incidence, considering the attenuation of EM waves in sea ice, the reflection and transmission coefficients of AB (shown in Figure 1) in the air-ice interface are:

$$F_{12H}^{1} = \frac{E_{s1H}^{1}}{E_i} = \frac{\tan(\theta_1 - \theta_2)}{\tan(\theta_1 + \theta_2)} = a \tag{A1}$$

$$T_{12H}^{1} = \frac{E_{t2H}^{1}}{E_i} = \frac{2\cos\theta_1 \sin\theta_2}{\sin(\theta_1 + \theta_2)\cos(\theta_1 - \theta_2)} = b \tag{A2}$$

For vertical polarization incidence, we have:

$$F_{12V}^{1} = \frac{E_{s1V}^{1}}{E_i} = \frac{\sin(\theta_2 - \theta_1)}{\sin(\theta_1 + \theta_2)} = c \tag{A3}$$

$$T_{12V}^{1} = \frac{E_{t2V}^{1}}{E_i} = \frac{2\cos\theta_1\sin\theta_2}{\sin(\theta_1+\theta_2)} = d \tag{A4}$$

When the first transmitted wave reaches the ice-water interface CD (shown in Figure 1), it is reflected and refracted again. The reflected wave vector is:

$$k_{s2}^{1} = k_2(\sin\theta_2 x_0 + \cos\theta_2 z_0) \tag{A5}$$

The transmitted wave vector propagating into the sea water should be:

$$k_{t3}^{1} = k_3(\sin\theta_2 x_0 - \cos\theta_2 z_0) \tag{A6}$$

Similarly, according to boundary conditions, $k_3$ is equal to $k_2$ and $k_0$. At the same time, we have:

$$\sin\theta_3 = \sqrt{\frac{\varepsilon_2}{\varepsilon_3}}\sin\theta_2 \tag{A7}$$

As with the reflection and transmission of the ice-air interface, the reflection and transmission coefficients of the interface CD are obtained. For horizontal polarization incidence, we have:

$$F_{23H}^{1} = \frac{E_{s2H}^{1}}{E_{t2H}^{1}\exp(-\alpha_2 r_2)} = \frac{\tan(\theta_2-\theta_3)}{\tan(\theta_2+\theta_3)} = e \tag{A8}$$

$$T_{23H}^{1} = \frac{E_{t3H}^{1}}{E_{t2H}^{1}\exp(-\alpha_2 r_2)} = \frac{2\cos\theta_2\sin\theta_3}{\sin(\theta_2+\theta_3)\cos(\theta_2-\theta_3)} = f \tag{A9}$$

For vertical polarization incidence, we have:

$$F_{23V}^{1} = \frac{E_{s2V}^{1}}{E_{t2V}^{1}\exp(-\alpha_2 r_2)} = \frac{\sin(\theta_3-\theta_2)}{\sin(\theta_2+\theta_3)} = g \tag{A10}$$

$$T_{23V}^{1} = \frac{E_{t3V}^{1}}{E_{t2V}^{1}\exp(-\alpha_2 r_2)} = \frac{2\cos\theta_3\sin\theta_2}{\sin(\theta_2+\theta_3)} = j \tag{A11}$$

When the reflected wave at the interface CD reaches the interface AB, it will reflect and refract again. Then, the reflection and transmission coefficients of the incident wave for horizontal polarization are:

$$F_{21H}^{1} = \frac{E_{t2H}^{2}}{E_{s2H}^{1}\exp(-\alpha_2 r_2)} = \frac{\tan(\theta_2-\theta_1)}{\tan(\theta_1+\theta_2)} = -a \tag{A12}$$

$$T_{21H}^{1} = \frac{E_{s1H}^{2}}{E_{s2H}^{1}\exp(-\alpha_2 r_2)} = \frac{2\cos\theta_2\sin\theta_1}{\sin(\theta_1+\theta_2)\cos(\theta_2-\theta_1)} = k \tag{A13}$$

For vertically polarized incident waves, we have:

$$F_{21V}^{1} = \frac{E_{t2V}^{2}}{E_{s2V}^{1}\exp(-\alpha_2 r_2)} = \frac{\sin(\theta_1-\theta_2)}{\sin(\theta_1+\theta_2)} = -c \tag{A14}$$

$$T_{21V}^{1} = \frac{E_{s1V}^{2}}{E_{s2V}^{1}\exp(-\alpha_2 r_2)} = \frac{2\cos\theta_2\sin\theta_1}{\sin(\theta_1+\theta_2)} = l \tag{A15}$$

When the reflected wave at the interface AB reaches the interface CD, the reflection and transmission coefficients of the incident wave for horizontal polarization will be:

$$F_{23H}^{2} = \frac{E_{s2H}^{2}}{E_{t2H}^{2}\exp(-\alpha_2 r_2)} = \frac{\tan(\theta_2-\theta_3)}{\tan(\theta_2+\theta_3)} = e \tag{A16}$$

$$T_{23H}^{2} = \frac{E_{t3H}^{2}}{E_{t2H}^{2}\exp(-\alpha_2 r_2)} = \frac{2\cos\theta_2\sin\theta_3}{\sin(\theta_2+\theta_3)\cos(\theta_2-\theta_3)} = f \tag{A17}$$

For vertical polarization, we have:

$$F_{23V}^{2} = \frac{E_{s2V}^{2}}{E_{t2V}^{2}\exp(-\alpha_2 r_2)} = \frac{\sin(\theta_3-\theta_2)}{\sin(\theta_2+\theta_3)} = g \tag{A18}$$

$$T_{23V}^{2} = \frac{E_{t3V}^{2}}{E_{t2V}^{2}\exp(-\alpha_2 r_2)} = \frac{2\cos\theta_3\sin\theta_2}{\sin(\theta_2+\theta_3)} = j \tag{A19}$$

For the nth incident wave at the interface AB, the reflection and transmission coefficients for horizontal polarization are:

$$F_{21H}^{n-1} = \frac{E_{t2H}^{n}}{E_{s2H}^{n-1}\exp(-\alpha_2 r_2)} = \frac{\tan(\theta_2-\theta_1)}{\tan(\theta_1+\theta_2)} = -a \tag{A20}$$

$$T_{21H}^{n-1} = \frac{E_{s1H}^{n}}{E_{s2H}^{n-1}\exp(-\alpha_2 r_2)} = \frac{2\cos\theta_2\sin\theta_1}{\sin(\theta_1+\theta_2)\cos(\theta_2-\theta_1)} = k \tag{A21}$$

For vertical polarization, they are:

$$F_{21V}^{n-1} = \frac{E_{t2V}^{n}}{E_{s2V}^{n}} = \frac{\sin(\theta_1-\theta_2)}{\sin(\theta_1+\theta_2)} = -c \tag{A22}$$

$$T_{21V}^{n-1} = \frac{E_{s1V}^{n}}{E_{s2V}^{n}} = \frac{2\cos\theta_2\sin\theta_1}{\sin(\theta_1+\theta_2)} = l \tag{A23}$$

For the nth incident wave at the interface CD, the reflection and transmission coefficients for horizontal polarization are:

$$F_{23H}^{n} = \frac{E_{s2H}^{n}}{E_{t2H}^{n}\exp(-\alpha_2 r_2)} = \frac{\tan(\theta_2-\theta_3)}{\tan(\theta_2+\theta_3)} = e \tag{A24}$$

$$T_{23H}^{n} = \frac{E_{t3H}^{n}}{E_{t2H}^{n}\exp(-\alpha_2 r_2)} = \frac{2\cos\theta_2\sin\theta_3}{\sin(\theta_2+\theta_3)\cos(\theta_2-\theta_3)} = f \tag{A25}$$

For vertical polarization, they are:

$$F_{23V}^{n} = \frac{E_{s2V}^{n}}{E_{t2V}^{n}\exp(-\alpha_2 r_2)} = \frac{\sin(\theta_3-\theta_2)}{\sin(\theta_2+\theta_3)} = g \tag{A26}$$

$$T_{23V}^{n} = \frac{E_{t3V}^{n}}{E_{t2}^{n}\exp(-\alpha_2 r_2)} = \frac{2\cos\theta_3\sin\theta_2}{\sin(\theta_2+\theta_3)} = j \tag{A27}$$

Considering formulas from (A1) to (A27) and with further calculation, when EM waves have first, second, third, …, nth time encounters with the interfaces, the electric field strength of scattering and transmission for different polarizations are as follows:

$$E_{s1H}^{1} = aE_i \tag{A28}$$

$$E_{t2H}^{1} = bE_i \tag{A29}$$

$$E_{s1V}^{1} = cE_i \tag{A30}$$

$$E_{t2V}^{1} = dE_i \tag{A31}$$

$$E_{s2H}^{1} = eE_{t2H}^{1}\exp(-\alpha_2 r_2) = beexp(-\alpha_2 r_2)E_i \tag{A32}$$

$$E_{t3H}^{1} = fE_{t2H}^{1}\exp(-\alpha_2 r_2) = bfexp(-\alpha_2 r_2)E_i \tag{A33}$$

$$E_{s2V}^{1} = gE_{t2V}^{1}\exp(-\alpha_2 r_2) = dgexp(-\alpha_2 r_2)E_i \tag{A34}$$

$$E_{t3V}^{1} = jE_{t2V}^{1}\exp(-\alpha_2 r_2) = djexp(-\alpha_2 r_2)E_i \tag{A35}$$

$$E_{t2H}^{2} = aE_{s2H}^{1}\exp(-\alpha_2 r_2) = -abeexp(-2\alpha_2 r_2)E_i \tag{A36}$$

$$E_{s1H}^{2} = kE_{s2H}^{1}\exp(-\alpha_2 r_2) = bekexp(-2\alpha_2 r_2)E_i \tag{A37}$$

$$E_{t2V}^{2} = cE_{s2V}^{1}\exp(-\alpha_2 r_2) = -cdgexp(-2\alpha_2 r_2)E_i \tag{A38}$$

$$E_{s1V}^{2} = lE_{s2V}^{1}\exp(-\alpha_2 r_2) = dglexp(-2\alpha_2 r_2)E_i \tag{A39}$$

$$E_{s2H}^{2} = eE_{t2H}^{2}\exp(-\alpha_2 r_2) = -abe^2exp(-3\alpha_2 r_2)E_i \tag{A40}$$

$$E_{t3H}^{2} = fE_{t2H}^{2}\exp(-\alpha_2 r_2) = -abefexp(-3\alpha_2 r_2)E_i \tag{A41}$$

$$E_{s2V}^{2} = gE_{t2V}^{2}\exp(-\alpha_2 r_2) = -cdg^2exp(-3\alpha_2 r_2)E_i \tag{A42}$$

$$E_{t3V}^{2} = jE_{t2V}^{2}\exp(-\alpha_2 r_2) = -cdgjexp(-3\alpha_2 r_2)E_i \tag{A43}$$

$$E_{t2H}^{3} = aE_{s2H}^{2}\exp(-\alpha_2 r_2) = a^2be^2exp(-4\alpha_2 r_2)E_i \tag{A44}$$

$$E_{s1H}^{3} = kE_{s2H}^{2}\exp(-\alpha_2 r_2) = -abe^2kexp(-4\alpha_2 r_2)E_i \tag{A45}$$

$$E_{t2V}^{3} = cE_{s2V}^{2}\exp(-\alpha_2 r_2) = c^2dg^2exp(-4\alpha_2 r_2)E_i \tag{A46}$$

$$E_{s1V}^{3} = lE_{s2V}^{2}\exp(-\alpha_2 r_2) = -cdg^2lexp(-4\alpha_2 r_2)E_i \tag{A47}$$

$$E_{s2H}^{3} = eE_{t2H}^{3}\exp(-\alpha_2 r_2) = a^2be^3exp(-5\alpha_2 r_2)E_i \tag{A48}$$

$$E_{t3H}^{3} = fE_{t2H}^{3}\exp(-\alpha_2 r_2) = a^2be^2fexp(-5\alpha_2 r_2)E_i \tag{A49}$$

$$E_{s2V}^{3} = gE_{t2V}^{3}\exp(-\alpha_2 r_2) = c^2dg^3exp(-5\alpha_2 r_2)E_i \tag{A50}$$

$$E_{t3V}^{3} = jE_{t2V}^{3}\exp(-\alpha_2 r_2) = c^2dg^2jexp(-5\alpha_2 r_2)E_i \tag{A51}$$

$$E_{t2H}^{n} = aE_{s2H}^{n-1}\exp(-\alpha_2 r_2) = (-ae)^{n-1}bexp(-2(n-1)\alpha_2 r_2)E_i \tag{A52}$$

$$E_{s1H}^{n} = kE_{s2H}^{n-1}\exp(-\alpha_2 r_2) = (-ae)^{n-2}bekE_i exp(-2(n-1)\alpha_2 r_2) \tag{A53}$$

$$E_{t2V}^{n} = cE_{s2V}^{n}\exp(-\alpha_2 r_2) = (-cg)^{n-1}dE_i exp(-2(n-1)\alpha_2 r_2) \tag{A54}$$

$$E_{s1V}^{n} = lE_{s2V}^{n}\exp(-\alpha_2 r_2) = (-cg)^{n-2}dglE_i exp(-2(n-1)\alpha_2 r_2) \tag{A55}$$

$$E_{s2H}^{n} = eE_{t2H}^{n}\exp(-\alpha_2 r_2) = (-ae)^{n-1}befE_i exp(-(2n-1)\alpha_2 r_2) \tag{A56}$$

$$E_{t3H}^{n} = fE_{t2H}^{n}\exp(-\alpha_2 r_2) = (-ae)^{n-1}bfE_i\exp(-(2n-1)\alpha_2 r_2) \quad \text{(A57)}$$

$$E_{s2V}^{n} = gE_{t2V}^{n}\exp(-\alpha_2 r_2) = (-cg)^{n-1}dgE_i\exp(-(2n-1)\alpha_2 r_2) \quad \text{(A58)}$$

$$E_{t3V}^{n} = jE_{t2}^{n}\exp(-\alpha_2 r_2) = (-cg)^{n-1}djE_i\exp(-(2n-1)\alpha_2 r_2) \quad \text{(A59)}$$

To summarize equations from (A28) to (A59), we can obtain the reflection coefficient of the ice-air interface for horizontal polarization:

$$\begin{aligned} S_{HH} &= \frac{E_{sH}}{E_i} = \frac{\sum_{n=1}^{+\infty} E_{s1H}^{n}}{E_i} \\ &= \{a + bek[1 + (-ae)\exp(-2\alpha_2 r_2) + (-ae)^2\exp(-4\alpha_2 r_2) \\ &\quad + \cdots (-ae)^{n-2}\exp(-2(n-1)\alpha_2 r_2) + \cdots]\} \\ &= a + \frac{bek}{1 + aeexp(-2\alpha_2 r_2)} \end{aligned} \quad \text{(A60)}$$

For vertical polarization, the reflection coefficient of the ice-air interface is:

$$\begin{aligned} S_{VV} &= \frac{E_{sV}}{E_i} = \frac{\sum_{n=1}^{+\infty} E_{s1V}^{n}}{E_i} \\ &= \{c + dgl[1 + (-cg)\exp(-2\alpha_2 r_2) + (-cg)^2\exp(-4r_2) \\ &\quad + \cdots (-cg)^{n-2}\exp(-2(n-1)\alpha_2 r_2) + \cdots]\} \\ &= c + \frac{dgl}{1 + cgexp(-2\alpha_2 r_2)} \end{aligned} \quad \text{(A61)}$$

The transmission coefficient of the ice-water interface for horizontal polarization is:

$$\begin{aligned} T_{HH} &= \frac{E_{tH}}{E_i} = \frac{\sum_{n=1}^{+\infty} E_{t3H}^{n}}{E_i} \\ &= bf[\exp(-\alpha_2 r_2) + (-ae)\exp(-3\alpha_2 r_2) + (-ae)^2\exp(-5\alpha_2 r_2) \\ &\quad + \cdots (-ae)^{n-1}\exp(-(2n-1)\alpha_2 r_2) + \cdots] \\ &= \frac{bfexp(-\alpha_2 r_2)}{1 + aeexp(-2\alpha_2 r_2)} \end{aligned} \quad \text{(A62)}$$

For vertical polarization, we have:

$$\begin{aligned} T_{VV} &= \frac{E_{tV}}{E_i} = \frac{\sum_{n=1}^{+\infty} E_{t3V}^{n}}{E_i} \\ &= dj[\exp(-\alpha_2 r_2) + (-cg)\exp(-3\alpha_2 r_2) + (-cg)^2\exp(-5\alpha_2 r_2) \\ &\quad + \cdots (-cg)^{n-2}\exp(-(2n-1)\alpha_2 r_2) + \cdots] \\ &= \frac{djexp(-\alpha_2 r_2)}{1 + cgexp(-2\alpha_2 r_2)} \end{aligned} \quad \text{(A63)}$$

Equations from (A60) to (A63) are the EMS and transmission models of floating sea ice, which can be used to derive the reflection and transmission coefficients for the VV and HH polarizations.

## References

Arcone S A, Gow A J and Mcgrew S. (1986). Structure and dielectric properties at 4.8 and 9.5 GHz of saline ice. *Journal of Geophysical Research Atmospheres*, 91(C12): 14281–14303. http://dx.doi.org/10.1029/JC091iC12p14281

Chow Y L, Hojjat N, Safavi-Naeini S, *et al*. (1998). Spectral Green's functions for multilayer media in a convenient computational form. *IEE Proceedings – Microwaves, Antennas and Propagation*, 145(1): 85–91. http://dx.doi.org/10.1049/ip-map:19981598

Cox G F N and Weeks W F. (1983). Equations for determining the gas and brine volumes in sea-ice samples. *Journal of Glaciology*, 29(102): 306–316. https://doi.org/10.1017/S0022143000008364

Ellison W, Balana A, Delbos G, *et al*. (1998). New permittivity measurements of seawater. *Radio Science*, 33(3): 639–648. http://dx.doi.org/10.1029/97RS02223

Engen G and Johnsen H. (1995). SAR-ocean wave inversion using image cross spectra. *IEEE Transactions on Geoscience and Remote Sensing*, 33(4): 1047–1056. http://dx.doi.org/10.1109/36.406690

Firoozy N, Komarov A S, Landy J, *et al*. (2015a). Inversion-based sensitivity analysis of snow-covered sea ice electromagnetic profiles. *IEEE Journal of Selected Topics in Applied Earth Observations and Remote Sensing*, 8(7): 3643–3655. http://dx.doi.org/10.1109/JSTARS.2015.2399651

Firoozy N, Komarov A S, Mojabi P, *et al*. (2016). Retrieval of young snow-covered sea-ice temperature and salinity evolution through radar cross-section inversion. *IEEE Journal of Oceanic Engineering*, 41(2): 326–338. http://dx.doi.org/ 10.1109/JOE.2015.2458212

Firoozy N, Mojabi P and Barber D G. (2015b). Nonlinear inversion of microwave scattering data for snow-covered sea-ice dielectric profile reconstruction. *IEEE Geoscience and Remote Sensing Letters*, 12(1): 209–213. http://dx.doi.org/10.1109/LGRS.2014.2332534

Franceschetti G, Imperatore P, Iodice A, *et al*. (2008). Scattering from layered structures with one rough interface: A unified formulation of perturbative solutions. *IEEE Transactions on Geoscience and Remote Sensing*, 46(6): 1634–1643. http://dx.doi.org/10.1109/TGRS.2008.916222

Francis J A and Vavrus S J. (2012). Evidence linking Arctic amplification to extreme weather in mid-latitudes. *Geophysical Research Letters*, 39(6): L06801. http://dx.doi.org/10.1029/2012GL051000

Gade M, Alpers W, Hühnerfuss H, *et al*. (1998). Imaging of biogenic and anthropogenic ocean surface films by the multifrequency/multipolarization SIR-C/X-SAR. *Journal of Geophysical Research Atmospheres*, 103(C9): 18851–18866. http://dx.doi.org/10.1029/97JC01915

Gao Y, Sun J, Li F, *et al*. (2015). Arctic sea ice and Eurasian climate: A review. *Advances in Atmospheric Sciences*, 32(1): 92–114. http://dx.doi.org/10.1007/s00376-014-0009-6

Golden K M, Borup D, Cheney M, *et al*. (1998). Forward electromagnetic scattering models for sea ice. *IEEE Transactions on Geoscience and Remote Sensing*, 36(5): 1655–1674. http:/dx.doi.org/10.1109/36.718638

Huntingford C, Jones P D, Livina V N, *et al*. (2013). No increase in global temperature variability despite changing regional patterns. *Nature*, 500(7462): 327–330. http:/dx.doi.org/10.1038/nature12310

Imperatore P, Iodice A and Riccio D. (2010). Physical meaning of perturbative solutions for scattering from and through multilayered structures with rough interfaces. *IEEE Transactions on Antennas and Propagation*, 58(8): 2710–2724. http://dx.doi.org/10.1109/TAP.2010.2050417

Imperatore P, Iodice A and Riccio D. (2011). Volumetric-perturbative reciprocal formulation for scattering from rough multilayers. *IEEE Transactions on Antennas and Propagation*, 59(3): 877–887. http://dx.doi.org/10.1109/TAP.2010.2103004

Imperatore P, Iodice A and Riccio D. (2012). Consistency and validity of perturbative formulations for scattering from rough multilayers. *IEEE Transactions on Antennas and Propagation*, 60(4): 2019–2027. http://dx.doi.org/10.1109/TAP.2012.2186267

Isleifson D, Jeffrey I, Shafai L, *et al*. (2012). A Monte Carlo method for simulating scattering from sea ice using FVTD. *IEEE Transactions on Geoscience and Remote Sensing*, 50(7): 2658–2668. http://dx.doi.org/10.1109/TGRS.2011.2173940

Komarov A S, Isleifson D, Barber D G, *et al*. (2015). Modeling and measurement of C-band radar backscatter from snow-covered first-year sea ice. *IEEE Transactions on Geoscience and Remote Sensing*, 53(7): 4063–4078. http://dx.doi.org/10.1109/TGRS.2015.2390192

Komarov A S, Shafai L and Barber D G. (2014). Electromagnetic wave scattering from rough boundaries interfacing inhomogeneous media and application to snow-covered sea ice. *Progress in Electromagnetics Research*, 144: 201–219. http://dx.doi.org/10.2528/PIER13111209

Kuang H L, Perrie W, Xie T, *et al*. (2012). Retrievals of sea surface temperature fronts from SAR imagery. *Geophysical Research Letters*, 39(10): L10607.

http://dx.doi.org/10.1029/2012GL051288

Li W L, Guo L X, Meng X, *et al*. (2014). Modeling and electromagnetic scattering from the overturning wave crest. *Acta Physica Sinica*, 63(16): 164102. http://dx.doi.org/10.7498/aps.63.164102

Nassar E M, Johnson J T and Lee R. (2000). A numerical model for electromagnetic scattering from sea ice. *IEEE Transactions on Geoscience and Remote Sensing*, 38(3): 1309–1319. http://dx.doi.org/10.1109/36.843024

Rahmstorf S and Coumou D. (2011). Increase of extreme events in a warming world. *Proceedings of the National Academy of Sciences of the United States of America*, 108(44): 17905–17909. http://dx.doi.org/10.1073/pnas.1101766108

Rosel A, Kaleschke L and Birnbaum G. (2012). Melt ponds on Arctic sea ice determined from MODIS satellite data using an artificial neural network. *The Cryosphere*, 6: 431–446. http://dx.doi.org/10.5194/tc-6-431-2012

Su T F, Li Y X and Li H Y. (2016). Sea oil spill detection method by SAR imagery using object-based image analysis and fuzzy logic. *Acta Oceanologica Sinica*, 38(1): 69–81. (in Chinese) http://dx.chinadoi.cn/10.3969%2fj.issn.0253-4193.2016.01.007

Vant M R, Ramseier R O and Makios V. (1978). The complex-dielectric constant of sea ice at frequencies in the range 0.1–40 GHz. *Journal of Applied Physics*, 49(3): 1264–1280. http://dx.doi.org/10.1063/1.325018

Wang L, Scott A, Xu L, *et al*. (2016a). Sea ice concentration estimation during melt from dual-pol SAR scenes using deep convolutional neural networks: A case study. *IEEE Transactions on Geoscience and Remote Sensing*, 54(8): 4524–4533. http://dx.doi.org/10.1109/TGRS.2016.2543660

Wang X S, Dai Q H, Jiao L C, *et al*. (2016b). Developments and prospects of high-performance detection imaging and identification. *Science China Information Sciences*, 46: 1211. http://dx.doi.org/10.1360/N112016-00111

Wang Y F, Liu C, Zhan X L, *et al*. (2016c). Technology and applications of UAV synthetic aperture radar system. *Journal of Radars*, 5(4): 333–349. (in Chinese) http://dx.doi.org/10.12000/JR16089

Xie T, Fang H, Zhao S Z, *et al*. (2015a). Analysis of the Arctic sea ice total deformation rates based on SAR remote sensing. *Acta Oceanologica Sinica*, 37(11): 118–126. (in Chinese) http://dx.doi.org/10.3969/j.issn.0253-4193.2015.11.011

Xie T, Perrie W and Chen W. (2010). Gulf Stream thermal fronts detected by synthetic aperture radar. *Geophysical Research Letters*, 37(6): L06601. http://dx.doi.org/10.1029/2009GL041972

Xie T, Perrie W, He Y J, *et al*. (2015b). Ocean surface wave measurements from fully polarimetric SAR imagery. *Science China Earth Sciences*, 58(10): 1849–1861. http://dx.doi.org/10.1007/s11430-015-5078-6

Xie T, Zhao S Z, Perrie W, *et al*. (2016). Electromagnetic backscattering from one-dimensional drifting fractal sea surface I: Wave-current coupled model. *Chinese Physics B*, 25(6): 064101. http://dx.doi.org/10.1088/1674-1056/25/6/064101

Zamani H, Tavakoli A and Dehmollaian M. (2016a). Scattering from layered rough surfaces: Analytical and numerical investigations. *IEEE Transactions on Geoscience and Remote Sensing*, 54(6): 3685–3696. http://dx.doi.org/10.1109/TGRS.2016.2524639

Zamani H, Tavakoli A and Dehmollaian M. (2016b). Second-order perturbative solution of cross-polarized scattering from multilayered rough surfaces. *IEEE Transactions on Antennas and Propagation*, 64(5): 1877–1890. http://dx.doi.org/10.1109/TAP.2016.2535503

Zhang X, Dierking W, Zhang J, *et al*. (2016). Retrieval of the thickness of undeformed sea ice from C-band compact polarimetric SAR images. *The Cryosphere*, 10: 1529–1545. http://dx.doi.org/10.5194/tc-10-1529-2016

Zhang X, Zhang J, Meng J M, *et al*. (2013). Polarimetric scattering characteristics based sea ice types classification by polarimetric synthetic aperture radar: Taking sea ice in the Bohai Sea for example. *Acta Oceanologica Sinica*, 35(5): 95–101. (in Chinese) http://dx.doi.org/10.3969/j.issn.0253-4193.2013.05.010

Zhao X B, Yan W, Kong Y, *et al*. (2013). Theoretical research and experimental verification for ocean surface wind vector retrieval from airborne C-band fully polarimetric SAR. *Acta Physica Sinica*, 62(13): 138402. http://dx.doi.org/10.7498/aps.62.138402Firoozy N, Mojabi P and Barber D G. (2015b). Nonlinear inversion of microwave scattering data for snow-covered sea-ice dielectric profile reconstruction. *IEEE Geoscience and Remote Sensing Letters*, 12(1): 209–213. http://dx.doi.org/10.1109/LGRS.2014.2332534